

Cell Reports Physical Science, Volume 5

Supplemental information

**Size-dependent magnon thermal transport
in a nanostructured quantum magnet**

Shucheng Guo, Hongze Li, Xue Bai, Yitian Wang, Shuchen Li, Rafal E. Dunin-Borkowski, Jianshi Zhou, and Xi Chen

Note S1: XRD analysis of samples before and after calcination

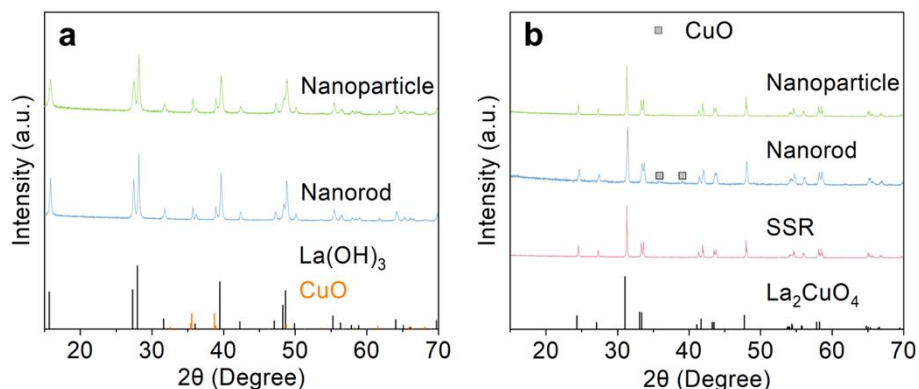


Figure S1. XRD patterns of La_2CuO_4 samples before and after calcination. (a) XRD patterns recorded from the La_2CuO_4 nanoparticle (NP) and nanorod (NR) samples after hydrothermal treatment. (b) XRD patterns recorded from the La_2CuO_4 NP and NR samples after calcination and La_2CuO_4 after solid state reaction (SSR).

Figure S1a shows that, following hydrothermal treatment, the La_2CuO_4 nanoparticle (NP) and nanorod (NR) samples have identical compositions, each consisting of $La(OH)_3$ (PDF#: 78-0190) and CuO (PDF#: 74-1021). Figure S1b shows that, after calcination, a La_2CuO_4 phase (PDF#: 82-2142) forms in both samples. In the NR sample, a trace amount of CuO impurity is observed. A pure La_2CuO_4 phase is formed in the sample prepared via solid state reaction (SSR).

Note S2: EDX characterization of La_2CuO_4 nanostructures

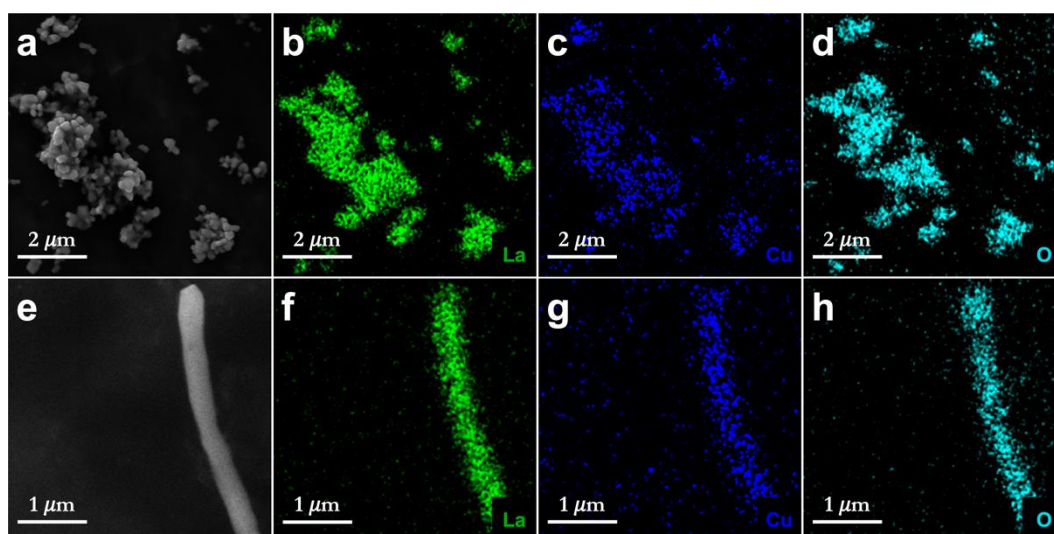


Figure S2. EDX characterization of La_2CuO_4 nanostructures. (a) SEM image of La_2CuO_4 nanoparticles after calcination. (b, c, d) Elemental distributions of La, Cu and O in the La_2CuO_4 nanoparticles. (e) SEM image of a La_2CuO_4 nanorod after calcination. (f, g, h) Elemental distributions of La, Cu and O in the La_2CuO_4 nanorod.

We used energy dispersive X-ray (EDX) analysis in a scanning electron microscope to examine elemental distributions in the La_2CuO_4 nanostructures after calcination. Figures S2a-d show EDX elemental mapping of the constituent elements (La, Cu and O), which exhibit chemical uniformity across the La_2CuO_4 nanoparticles. Figures S2e-h show even distributions of La, Cu and O in individual La_2CuO_4 nanorods.

Note S3: Effect of heating rate on La_2CuO_4 nanorod morphology

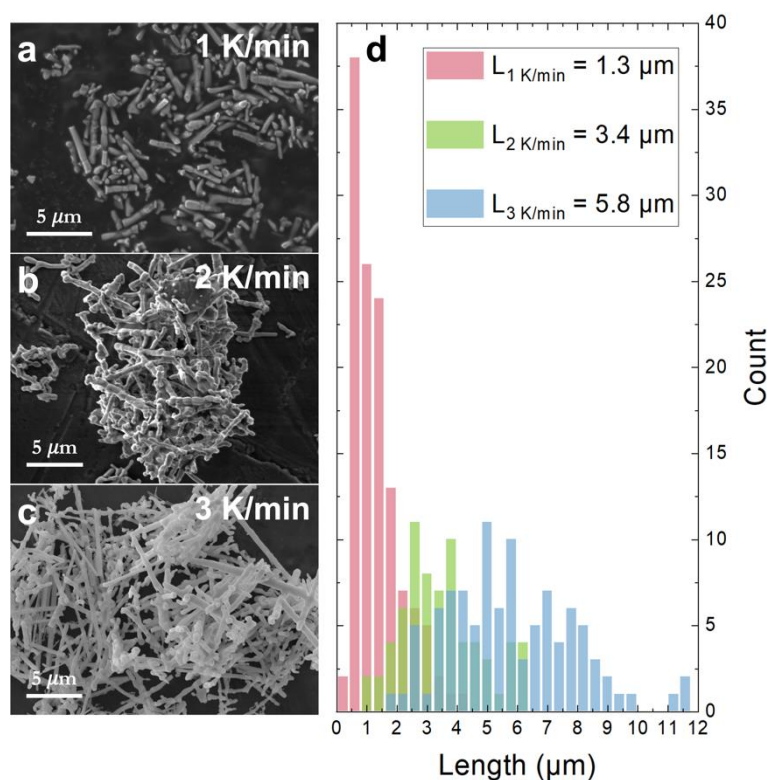


Figure S3. Effect of heating rate on La_2CuO_4 nanorod morphology. (a, b, c) SEM images of La_2CuO_4 nanorods that had been subjected to different heating rates during calcination. The scale bars are all 5 μm . (d) Distributions of nanorod lengths for different heating rates.

The calcination process involved two steps. In the first step, the hydrothermal product was calcined in air at a heating rate of 1 K/min from room temperature to 400 $^{\circ}\text{C}$. The sample was kept at this temperature for 1 h. The second step involved further heating of the solid at rates of 1-3 K/min to 850 $^{\circ}\text{C}$. The sample was then maintained at 850 $^{\circ}\text{C}$ for 6 h. A noteworthy observation is that the heating rates in the second step seemed to affect the length and surface smoothness of the La_2CuO_4 nanorods. Figures S3a-c show that the use of higher heating rates leads to the formation of more elongated nanorods with smoother surfaces. Figure S3d shows that the average nanorod lengths are 1.3, 3.4 and 5.8 μm for heating rates of 1, 2 and 3 K/min, respectively. Figure S3b also reveals the presence of some nano-bamboo structures. Unlike the nanorods, the nano-bamboos have shorter lengths and coarser surface textures. These features are attributed to the slower heating rate applied during calcination, which leads to fragmentation in the nanostructures. Therefore, a more rapid heating rate results in an optimal surface energy, favoring the growth of longer and smoother nanorods.

Note S4: TEM characterization of a La_2CuO_4 nano-bamboo

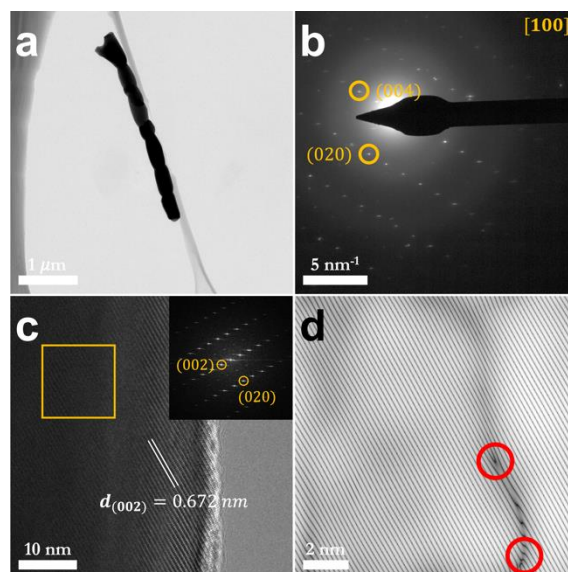


Figure S4. TEM characterization of a La_2CuO_4 nano-bamboo. (a) Bright-field TEM image of a nano-bamboo structure prepared at a heating rate of 2 K/min. The scale bar is 1 μm . (b) Selected area electron diffraction pattern recorded from the nano-bamboo structure in (a). The scale bar is 5 nm^{-1} . (c) High-resolution TEM image. The scale bar is 10 nm. The inset shows a fast Fourier transform (FFT). (d) Filtered inverse FFT of the marked area in (c). The scale bar is 2 nm.

Transmission electron microscopy (TEM) was used to characterize the La_2CuO_4 nano-bamboos. Figure S4a shows a nano-bamboo that is composed of several grains, linked by distinct grain boundaries, culminating in a bamboo-like morphology with an approximate length of 3.3 μm . Figure S4b shows a selected area electron diffraction pattern, which confirms that each grain is a single crystal. Figure S4d shows a filtered inverse FFT of the $20 \times 20 \text{ nm}^2$ region marked in the high-resolution TEM image in Figure. S4c, in which several dislocations indicated by red circles are visible. It is important to note that uniform heating of all solids cannot be guaranteed during the calcination process. As a result, even when applying a heating rate of 3 K/min, there is still a possibility of nano-bamboo formation. The presence of defects in the nano-bamboos may reduce the thermal conductivity of the sample.

Note S5: EDX mapping of samples after SPS

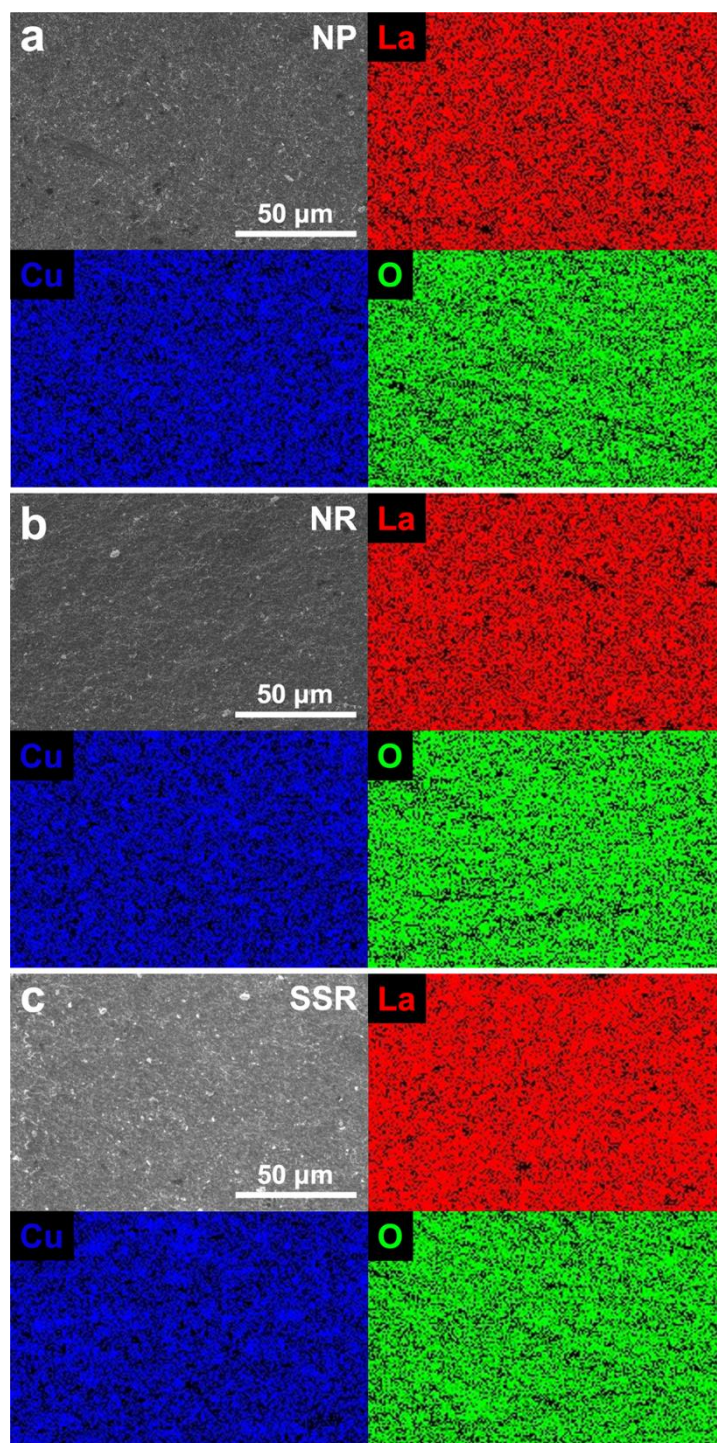


Figure S5. SEM images and element mapping by EDX. (a) NP, (b) NR, and (c) SSR samples after SPS. The scale bars are all 50 μm.

As shown in Figure S5, SEM images were obtained for the NP, NR, and SSR samples after SPS. The samples exhibit homogeneity in microstructure. Furthermore, all three elements, La, Cu, and O, are uniformly distributed in the three samples, as confirmed by the EDX study.

Note S6: Raman spectra below 1500 cm^{-1}

As illustrated in the Figure S6, the Raman spectra between 750 and 1500 cm^{-1} are represented by the pink shaded area, while the yellow shaded area corresponds to the spectra below 750 cm^{-1} . The dashed lines within the pink area indicate the two-phonon bands of La_2CuO_4 , while the dashed line in the yellow area delineates the one-phonon bands. The labeled peak positions are consistent with previous Raman studies.^{1,2} It is noted that there are some discrepancies in the intensity of the Raman peaks compared to the previous work, which could be due to differences in laser beam energy.

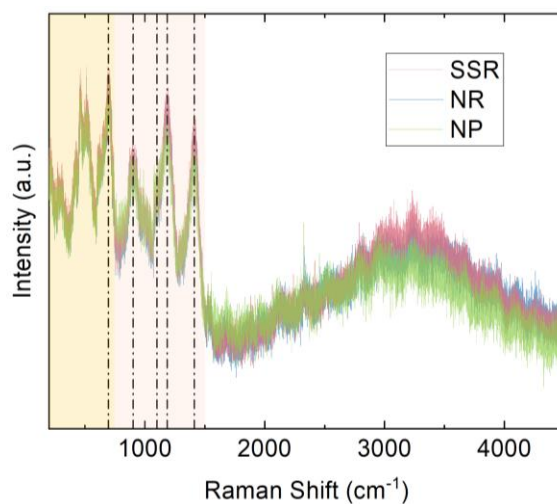


Figure S6. Raman spectra recorded from the SSR, NR and NP samples after SPS treatment, excited by a 532 nm laser. Pink shaded area represents the Raman shift between 750 and 1500 cm^{-1} . Yellow shaded area shows to the Raman shift below 750 cm^{-1} .

Note S7: Thermal conductivity measurements and uncertainty analysis

The samples were cut to standard dimensions of $1.5 \times 1.5 \times 8 \text{ mm}^3$ for measurements of thermal conductivity (κ) using a Quantum Design Physical Property Measurement System (PPMS) operated in a steady-state 4-probe continuous mode. The measurements were carried out over a temperature range of 3 to 350 K. Data acquisition was performed continuously at a low heating rate of 0.3 K min^{-1} . The software automatically adjusted other measurement parameters, such as the heating power and period.³ A square wave heat pulse was administered, and the resulting temperature difference between the hot and cold probes was measured over time. The steady state temperature difference was determined by fitting the data using the expression

$$\Delta T = \Delta T_{\infty} \times \left(1 - \frac{\tau_1 \times \exp\left(-\frac{t}{\tau_1}\right) - \tau_2 \times \exp\left(-\frac{t}{\tau_2}\right)}{\tau_1 - \tau_2}\right), \quad (1)$$

where ΔT is the measured temperature difference, ΔT_{∞} is the steady-state temperature difference, and τ_1 and τ_2 are time constants. Once ΔT_{∞} has been determined, the thermal conductance (K) can be calculated from the following equations:

$$K = P / \Delta T_{\infty} \quad (2)$$

$$P = I^2 R - P_{rad} \quad (3)$$

$$P_{rad} = \sigma_T \times \left(\frac{S}{2}\right) \times \varepsilon \times (T_{hot}^4 - T_{cold}^4) \quad , \quad (4)$$

where P is the heat flowing through the sample, I is the current flowing into the sample, R is the resistance of the heater, $\sigma_T = 5.67 \times 10^{-8} \text{ Wm}^{-2}\text{K}^{-4}$ is the Stefan-Boltzmann constant, S is the surface area of the sample, ε is the emissivity, and T_{hot} and T_{cold} are the temperatures of the hot and cold probes, respectively. The value of κ can then be obtained from the expressions

$$\kappa = K_{sample} \times l / (w \times t) \quad (5)$$

$$K_{sample} = K - K_{shoe} \quad (6)$$

$$K_{shoe} = aT + bT^2 + cT^3 \quad , \quad (7)$$

where K_{sample} and K_{shoe} are the thermal conductance of the sample and the thermal conductance of the shoe assembly, respectively, a , b and c are constants, and l , w and t are the distance between the hot and cold probes and the width and thickness of the sample, separately. The measurement of κ is subject to errors from multiple origins. These include errors in the fitting of ΔT , uncertainties in the measurement of the heating power, and inaccuracies in estimating radiation losses due to errors in sample surface area and emissivity. Based on the PPMS measurements, the surface radiation heat loss from the La_2CuO_4 samples is calculated to be less than 0.4% of the heat conduction in the La_2CuO_4 . Furthermore, it is crucial to account for errors in K_{shoe} , as well as in measurements of the sample size and distance (d) between the hot and cold probes. The total error can be expressed as follows:

$$\sigma(\kappa) = \kappa \times \sqrt{\left(\frac{R_{\Delta T}}{\Delta T_{\infty}}\right)^2 + \left(2 \frac{IR\partial I}{P}\right)^2 + \left(\frac{0.2 \times P_{rad}}{P}\right)^2 + \left(\frac{0.1 \times T_{\infty} \times K_{shoe}}{P}\right)^2 + \left(\frac{\Delta l}{l}\right)^2 + \left(\frac{\Delta w}{w}\right)^2 + \left(\frac{\Delta t}{t}\right)^2} \quad , \quad (8)$$

where $R_{\Delta T}$ is a residual term from the fitting of ΔT versus t .

Note S8: Texture of the NR sample after spark plasma sintering

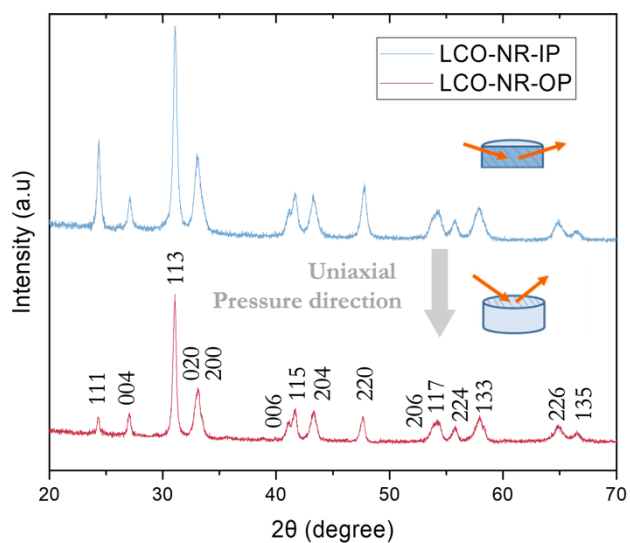


Figure S7. XRD patterns of La_2CuO_4 NPs after SPS taken on planes parallel and perpendicular to the press direction.

In order to investigate the texture of the NR sample after spark plasma sintering (SPS), XRD analysis was performed on planes parallel (in-plane, IP) and perpendicular (out-of-plane, OP) to the press direction, as shown in Figure. S7. The diffraction intensity of the (111) peak measured on the plane parallel to the press direction is much stronger than that on the plane perpendicular to the press direction. Given that the growth direction of the La_2CuO_4 nanorods is [111], the anisotropy observed in the XRD patterns can be attributed to the NRs having a greater tendency to align along the in-plane direction during SPS.

Note S9: Correction for porosity effect

The Maxwell-Eucken relation is a useful theoretical model for determining the thermal conductivity of composite materials, especially useful for materials made up of a two-phase mixture, such as a porous medium.⁴ Based on the Maxwell-Eucken relation, the equation for eliminating the impact of porosity on thermal transport can be expressed as follows:⁵

$$\kappa = \kappa_s \frac{\kappa_p + 2\kappa_s + 2\Phi(\kappa_p - \kappa_s)}{\kappa_p + 2\kappa_s - \Phi(\kappa_p - \kappa_s)}, \quad (9)$$

where κ represents the measured thermal conductivity, κ_p is the thermal conductivity of pores, Φ denotes the porosity, and κ_s is the solid thermal conductivity, assumed to be the value when the porosity is 0. Generally, accurately obtaining κ_p is challenging due to the influence of external factors, such as air and moisture. However, our measurements were conducted under ultra-high vacuum conditions. This ensures that the pores do not contribute to heat conduction, allowing us to consider $\kappa_p = 0$. Therefore, equation 4 in the main text can be simplified as:

$$\kappa_s = \kappa \frac{2 + \Phi}{2 - 2\Phi}. \quad (10)$$

In addition, Smith et al.⁵ have verified that when Φ is smaller than 0.65, this relation shows good agreement with experimental data on several oxides. Meanwhile, the Maxwell-Eucken relation has been widely used in many material systems,⁶⁻¹⁶ with porosity comparable to that of our samples. Given that the porosity of the SSR, NR, and NP samples in our study are 25%, 16%, and 10% respectively, all significantly lower than 65%, this relation can offer a reasonable correction for the effect of porosity in our samples.

Note S10: Fitting of lattice thermal conductivity using the Debye-Callaway model

Based on the previous study by Hess *et al.*¹⁷, the contribution to κ from magnons is negligible below ~ 50 K, with phonon transport then dominating. Therefore, we fitted the κ data at lower temperatures to the Debye-Callaway model for 3D phonon transport and extrapolated the fitting results at higher temperatures¹⁸

$$\kappa_L = \frac{k_B}{2\pi^2 v_s} \left(\frac{k_B T}{\hbar} \right)^3 \int_0^{\theta_D/T} \frac{x^4 e^x}{\tau_p^{-1} (e^x - 1)^2} dx \quad , \quad (11)$$

where κ_L is the lattice thermal conductivity, k_B is the Boltzmann constant, v_s is the sound velocity, \hbar is the reduced Planck constant, θ_D is the Debye temperature, and $x = \frac{\hbar\omega}{k_B T}$. The

specific heat (C_p) of the sample is fitted by the following equations:

$$\frac{C_p}{T} = \frac{\gamma}{M} + \frac{12\pi^4 N k_B}{5M\theta_D^3} T^2 \quad (12)$$

$$\theta_D = \frac{\hbar v_s}{k_B} \cdot \left(\frac{6\pi^2 N}{V} \right)^{1/3} \quad , \quad (13)$$

where γ is the electronic heat capacity coefficient, M is the molar mass, N is the number of atoms per unit cell, and V is the unit cell volume.

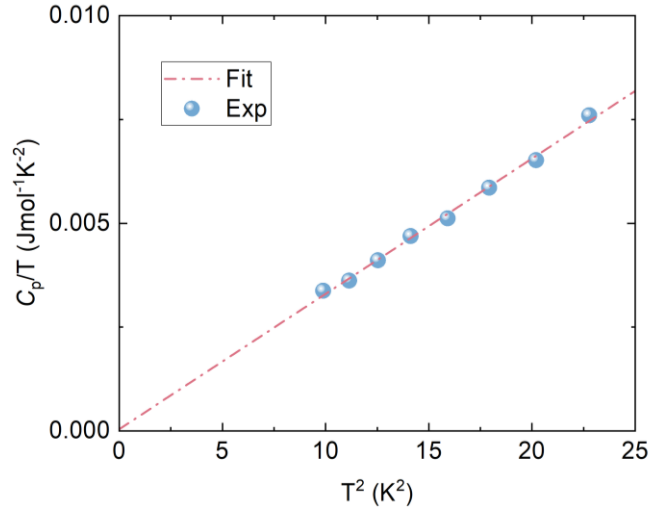


Figure S8. Experimental and fitting results of C_p/T versus T^2 at lower temperatures.

Based on the fitting results shown in Figure S8, θ_D was found to be 307 K, with v_s equal to 3073 ms^{-1} . The phonon relaxation time τ_p can be affected by various scattering processes, including defect scattering, Umklapp scattering, and boundary scattering. According to Matthiessen's rule, τ_p can be expressed in the form

$$\tau_p^{-1} = \tau_d^{-1} + \tau_U^{-1} + \tau_b^{-1} = A\omega^4 + B e^{-b/T} T^3 \omega^2 + \frac{v_s}{L} \quad , \quad (14)$$

where A is the fitting parameter for defect scattering, B and b are fitting parameters for Umklapp scattering, and L is the phonon-boundary scattering mean free path (MFP). The obtained fitting parameters are listed in Table S1.

Table S1. Fitting parameters of the Debye-Callaway model for six La_2CuO_4 polycrystalline samples and two reported single crystals.

| Sample | A (s^3) | B ($s \cdot K^{-3}$) | b (K) | L (m) |
|--------------|-------------------------|--------------------------|---------|------------------------|
| LCO-SSR-IP | 0.824×10^{-42} | 3.814×10^{-18} | 46.082 | 9.851×10^{-7} |
| LCO-SSR-OP | 0.753×10^{-42} | 5.013×10^{-18} | 35.342 | 9.254×10^{-7} |
| LCO-NR-IP | 1.902×10^{-42} | 5.826×10^{-18} | 45.018 | 6.958×10^{-7} |
| LCO-NR-OP | 2.635×10^{-42} | 7.817×10^{-18} | 34.217 | 4.714×10^{-7} |
| LCO-NP-IP | 1.651×10^{-42} | 8.074×10^{-18} | 40.513 | 4.732×10^{-7} |
| LCO-NP-OP | 3.078×10^{-42} | 8.132×10^{-18} | 53.072 | 4.604×10^{-7} |
| LCO-xtl-Hess | 3.056×10^{-42} | 4.712×10^{-18} | 39.324 | 3.702×10^{-6} |
| LCO-xtl-Sun | 8.156×10^{-43} | 7.213×10^{-18} | 39.071 | 3.743×10^{-6} |

Note S11: Reliability of the Debye-Callaway model

In order to justify the use of the “extrapolating” approach, we tested this method on the thermal conductivity of La_2CuO_4 along the c -axis, where thermal transport is predominantly phonon-driven. Initially, we fitted the thermal conductivity data between 2 K and 50 K using the Debye-Callaway model. This fitting was then extrapolated to higher temperatures, ranging from 50 to 300 K. As shown in Figure S9, the extrapolated curve closely aligns with the experimental data, with negligible deviations. Additionally, the fitting parameters obtained for phonon-phonon scattering are comparable to those for thermal conductivity along the ab plane. These results suggest that our approach for determining the lattice thermal conductivity at high temperatures is reasonable. Furthermore, this method has also been employed in several previous studies to estimate κ_L and analyze magnon thermal transport in various magnetic materials.^{17,19–24}

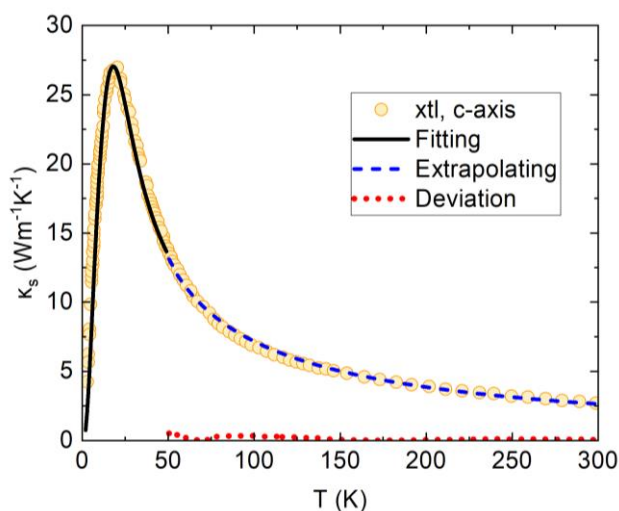


Figure S9. Thermal conductivity of single crystal (xtl) data along the c -axis.²⁵ The black solid line represents the fitting results of the lattice thermal conductivity based on the Debye-Callaway model, where $A = 10.556 \cdot 10^{-43} \text{ s}^3$, $B = 8.7136 \cdot 10^{-18} \text{ s} \cdot \text{K}^{-3}$, $b = 59.071 \text{ K}$, and $L = 3.743 \cdot 10^{-6} \text{ m}$. The blue dashed line shows the results by extrapolating the fitting to high temperatures. The red dotted line shows the deviation between the experimental data and the extrapolated results in the temperature range of 50 to 300 K.

Note S12: Equations for intrinsic magnon thermal conductivity

The magnon thermal conductivity can be obtained using the following equation:¹⁷

$$\kappa_m = \kappa_s - \kappa_L, \quad (15)$$

where κ_m is the thermal conductivity contributed by magnons, κ_s is the solid thermal conductivity, and κ_L is the lattice thermal conductivity contributed by phonons. Since La_2CuO_4 is an insulator, the contribution of electrons to thermal conductivity can be ignored. The dominant heat carriers in this material are phonons and magnons. The solid thermal conductivity is, therefore, the sum of the magnon and lattice thermal conductivities. Consequently, the magnon thermal conductivity can be determined by subtracting the lattice thermal conductivity from the solid thermal conductivity.

In La_2CuO_4 , the intrinsic magnon thermal conductivity (κ_m^i) along the ab plane can be calculated as:¹⁷

$$\kappa_m^i = \frac{3}{2}(\kappa^{poly} - \kappa_L^{poly}) = \frac{3}{2}\kappa_m^{poly} = \frac{3}{2} \frac{(2\kappa_{m,IP} + \kappa_{m,OP})}{3}, \quad (16)$$

where κ^{poly} , κ_L^{poly} , κ_m^{poly} are the thermal conductivity, lattice thermal conductivity, and magnon thermal conductivity of polycrystals, respectively. Additionally, $\kappa_{m,IP}$ and $\kappa_{m,OP}$ denote the magnon thermal conductivities obtained from samples cut parallel (in-plane, IP) and perpendicular (out-of-plane, OP), respectively, to the Spark Plasma Sintering (SPS) uniaxial pressure direction. The specific derivation process of equation 16 is as follows:

In polycrystals, since the crystal orientation of each grain is randomly distributed, the polycrystalline thermal conductivity can be treated as the average value of the thermal conductivity along the a -, b -, and c -axes:

$$\kappa^{poly} = \frac{(\kappa_a + \kappa_b + \kappa_c)}{3}, \quad (17)$$

$$\kappa_L^{poly} = \frac{(\kappa_{a,L} + \kappa_{b,L} + \kappa_{c,L})}{3}, \quad (18)$$

where κ_a , κ_b , and κ_c represent the values of thermal conductivity along the a -, b -, and c -axes, respectively, and $\kappa_{a,L}$, $\kappa_{b,L}$, and $\kappa_{c,L}$ are the values of lattice thermal conductivity along the a -, b -, and c -axes, separately. In addition, since La_2CuO_4 exhibits a 2D magnetic structure with its spin-plane (ab -plane) possessing extremely high symmetry, the value of κ_c is determined only by phonons. This indicates that $\kappa_c = \kappa_{c,L}$, and the contribution of magnons along the c -axis is zero ($\kappa_{c,m} = 0$). In contrast, the value of κ in the ab -plane (κ_{ab}) is uniform,^{26,27} involving both phonons ($\kappa_{ab,L}$) and magnons ($\kappa_{ab,m}$) in thermal transport. This implies that the κ along both a - and b -axes are identical to κ_{ab} :

$$\kappa_a = \kappa_b = \kappa_{ab}, \quad (19)$$

$$\kappa_{a,L} = \kappa_{b,L} = \kappa_{ab,L}, \quad (20)$$

$$\kappa_{a,m} = \kappa_{b,m} = \kappa_{ab,m}. \quad (21)$$

Furthermore, due to its unique spin-plane structure, the maximum capacity of La_2CuO_4 for magnon-based thermal transport can only be realized in the ab -plane. This implies:

$$\kappa_m^i = \kappa_{ab,m}. \quad (22)$$

Therefore κ_m^{poly} can be expressed as:

$$\kappa_m^{poly} = \kappa^{poly} - \kappa_L^{poly} = \frac{(\kappa_a + \kappa_b + \kappa_c)}{3} - \frac{(\kappa_{a,L} + \kappa_{b,L} + \kappa_{c,L})}{3} = \frac{(2\kappa_{ab} + \kappa_c)}{3} - \frac{(2\kappa_{ab,L} + \kappa_{c,L})}{3}$$

$$= \frac{(2\kappa_{ab,L} + 2\kappa_{ab,m} + \kappa_c)}{3} - \frac{(2\kappa_{ab,L} + \kappa_{c,L})}{3} = \frac{2\kappa_{ab,m}}{3} = \frac{2\kappa_m^i}{3}. \quad (23)$$

The polycrystalline thermal conductivity can be directly measured in polycrystal samples. However, the SPS process can induce anisotropy between directions parallel and perpendicular to the SPS uniaxial pressure. In order to mitigate the inaccuracies caused by this anisotropy, it's necessary to measure the thermal conductivity in three mutually perpendicular directions. One of these directions is out-of-plane, and the other two are in-plane but perpendicular to each other. Averaging the values obtained from these directions provides a more accurate representation of the polycrystalline thermal conductivity. As the SPS process does not introduce anisotropy in the in-plane directions, the thermal conductivity is uniform across these in-plane directions. Therefore, κ_m^{poly} can also be expressed as:

$$\kappa_m^{poly} = \kappa^{poly} - \kappa_L^{poly} = \frac{(2\kappa_{IP} + \kappa_{OP})}{3} - \frac{(2\kappa_{L,IP} + \kappa_{L,OP})}{3} = \frac{(2\kappa_{m,IP} + \kappa_{m,OP})}{3}, \quad (24)$$

where κ_{IP} and κ_{OP} represent the thermal conductivities measured from the in-plane and out-of-plane directions of the sample, respectively, while $\kappa_{L,IP}$ and $\kappa_{L,OP}$ are the lattice thermal conductivities of the in-plane and out-of-plane directions, separately.

In summary:

$$\begin{aligned} \kappa_m^{poly} &= \kappa^{poly} - \kappa_L^{poly} = \frac{(2\kappa_{m,IP} + \kappa_{m,OP})}{3} = \frac{2\kappa_{ab,m}}{3} = \frac{2\kappa_m^i}{3}, \\ \rightarrow \kappa_m^i &= \frac{3}{2}(\kappa^{poly} - \kappa_L^{poly}) = \frac{3}{2}\kappa_m^{poly} = \frac{3}{2}\frac{(2\kappa_{m,IP} + \kappa_{m,OP})}{3}, \end{aligned} \quad (16)$$

Note S13: Magnon thermal conductivity calculation

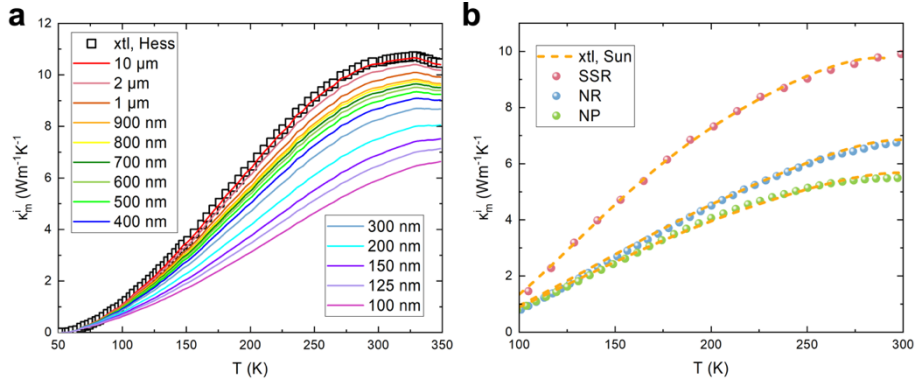


Figure S10. Magnon thermal conductivity calculation. (a) Calculated magnon thermal conductivity of La_2CuO_4 with various grain sizes using equations 7 and 8 in the main text. Black open squares represent the magnon thermal conductivity of the La_2CuO_4 single crystal (xtl) data along the ab -plane reported by Hess et al.¹⁷ (b) Fitting of the intrinsic magnon thermal conductivity of the SSR, NR and NP samples using equations 7 and 9 in the main text by considering boundary and defect scattering based on the La_2CuO_4 single-crystal (xtl) data along the ab -plane reported by Sun et al.²⁵

In order to explore the correlation between magnon thermal conductivity (κ_m) and grain size, κ_m was calculated over the temperature range 50 to 350 K for various grain sizes. The calculations incorporated the magnon-boundary scattering MFP (l_b) in the expression for the total magnon MFP using equations 7 and 8 from the main text. Figure S10a shows that, in the absence of additional defect scattering, the value of κ_m for a sample with a value of l_b of 10 μm does not show a significant variation compared to a single crystal. Suppression of l_b to 100 nm can reduce κ_m by nearly half.

We used equations 7 and 9 in the main text, which consider both boundary and defect scattering, to account for the presence of defects in the samples. As discussed in the main text, the magnon-defect scattering MFP should follow the expression $l_d^{-1} = c_d k^3$ for 2D magnon transport in spin-plane compounds, where c_d is a constant. Figure S10 shows that, after accounting for both boundary and defect scattering, good agreement is achieved between our experimental results and the fits over the temperature range 100 to 300 K.

References

1. Liu, Y., Wan, S. L., and Li, X. G. (2007). Excess oxygen doping in chemically oxidized $\text{La}_2\text{CuO}_{4+\delta}$ films studied by x-ray diffraction and Raman scattering. *Supercond. Sci. Technol.* *20*, 870. 10.1088/0953-2048/20/8/025.
2. Sugai, S. (1989). Phonon Raman scattering in $(\text{La}_{1-x}\text{Sr}_x)_2\text{CuO}_4$ single crystals. *Phys. Rev. B.* *39*, 4306. 10.1103/PhysRevB.39.4306.
3. Maldonado, O. (1992). Pulse method for simultaneous measurement of electric thermopower and heat conductivity at low temperatures. *Cryogenics (Guildf)* *32*, 908–912. 10.1016/0011-2275(92)90358-H.
4. Levy, F. L. (1981). A modified Maxwell-Eucken equation for calculating the thermal conductivity of two-component solutions or mixtures. *Int. J. Refrig.* *4*, 223–225. 10.1016/0140-7007(81)90053-0.
5. Smith, D. S., Alzina, A., Bourret, Julie., Nait-Ali, B., Pennec, F., Tessier-Doyen, N., Otsu, K., Matsubara, H., Elser, P., and Gonzenbach, U. T. (2013). Thermal conductivity of porous materials. *J. Mater. Res.* *28*, 2260–2272. 10.1557/jmr.2013.179.
6. Zhao, S., Zhu, R., and Fu, Y. (2019). Piezothermic Transduction of Functional Composite Materials. *ACS Appl. Mater. Interfaces.* *11*, 4588–4596. 10.1021/acsami.8b18639.
7. Nautiyal, P., Zhang, C., Loganathan, A., Boesl, B., and Agarwal, A. (2019). High-Temperature Mechanics of Boron Nitride Nanotube “Buckypaper” for Engineering Advanced Structural Materials. *ACS Appl. Nano. Mater.* *2*, 4402–4416. 10.1021/acsanm.9b00817.
8. Yu, P., Duan, Y. H., Chen, E., Tang, S. W., and Wang, X. R. (2018). Microstructure-based fractal models for heat and mass transport properties of cement paste. *Int. J. Heat. Mass. Transf.* *126*, 432–447. 10.1016/j.ijheatmasstransfer.2018.05.150.
9. Nomura, A., Choi, S., Ishimaru, M., Kosuga, A., Chasapis, T., Ohno, S., Jeffrey Snyder, G., Ohishi, Y., Muta, H., Yamanaka, S., et al. (2018). Chalcopyrite ZnSnSb_2 : A Promising Thermoelectric Material. *ACS Appl. Mater. Interfaces.* *10*, 43682–43690. 10.1021/acsami.8b16717.
10. Burgos-Mármol, J. J., and Patti, A. (2017). Unveiling the impact of nanoparticle size dispersity on the behavior of polymer nanocomposites. *Polymer (Guildf)* *113*, 92–104. 10.1016/j.polymer.2017.01.081.
11. Radu, A. I., Defraeye, T., Ruch, P., Carmeliet, J., and Derome, D. (2017). Insights from modeling dynamics of water sorption in spherical particles for adsorption heat pumps. *Int. J. Heat. Mass. Transf.* *105*, 326–337. 10.1016/j.ijheatmasstransfer.2016.09.079.
12. Kroon, R., Ryan, J. D., Kiefer, D., Yu, L. Y., Hynynen, J., Olsson, E., and Müller, C. (2017). Bulk Doping of Millimeter-Thick Conjugated Polymer Foams for Plastic Thermoelectrics. *Adv. Funct. Mater.* *27*, 1704183. 10.1002/adfm.201704183
13. Rannabauer, S., Söffker, G., Scheunemann, M., Betke, U., and Scheffler, M. (2017). Increased Mechanical Stability and Thermal Conductivity of Alumina Reticulated Porous Ceramics (RPC) by Nanoparticle Infiltration Processing. *Adv. Eng. Mater.* *19*, 1700211. 10.1002/adem.201700211.
14. Zhang, Y. K., Han, Z. S., Yu, Y. S., Rhamdhani, M. A., Gao, Y. M., and Guo, C. S. (2024). Research on the effective thermal conductivity of nickel-based bi-porous capillary wicks: Modeling and validation. *Int. J. Heat. Mass. Transf.* *218*, 124776. 10.1016/j.ijheatmasstransfer.2023.124776.

15. Ying, Y., Yang, G., Tao, Y., Wu, Q., and Li, H. (2023). Synergistically Enabling Fast-Cycling and High-Yield Atmospheric Water Harvesting with Plasma-Treated Magnetic Flower-Like Porous Carbons. *Adv. Sci.* *10*, 2204840. 10.1002/adv.202204840.
16. Østergaard, M. B., Zhang, M. L., Shen, X. M., Petersen, R. R., König, J., Lee, P. D., Yue, Y. Z., and Cai, B. (2020). High-speed synchrotron X-ray imaging of glass foaming and thermal conductivity simulation. *Acta. Mater.* *189*, 85–92. 10.1016/j.actamat.2020.02.060.
17. Hess, C., Büchner, B., Ammerahl, U., Colonescu, L., Heidrich-Meisner, F., Brenig, W., and Revcolevschi, A. (2003). Magnon Heat Transport in Doped La_2CuO_4 . *Phys. Rev. Lett.* *90*, 4. 10.1103/PhysRevLett.90.197002.
18. Sologubenko, A. V., Giannó, K., Ott, H. R., Ammerahl, U., and Revcolevschi, A. (2000). Thermal Conductivity of the Hole-Doped Spin Ladder System $\text{Sr}_{14-x}\text{Ca}_x\text{Cu}_{24}\text{O}_{41}$. *Phys. Rev. Lett.* *84*, 2714–2717. 10.1103/PhysRevLett.84.2714.
19. Hofmann, M., Lorenz, T., Berggold, K., Grüninger, M., Freimuth, A., Uhrig, G. S., and Brück, E. (2003). Evidence for a large magnetic heat current in insulating layered cuprates. *Phys. Rev. B.* *67*, 184502. 10.1103/PhysRevB.67.184502.
20. Hess, C., ElHaes, H., Waske, A., Büchner, B., Sekar, C., Krabbes, G., Heidrich-Meisner, F., and Brenig, W. (2007). Linear Temperature Dependence of the Magnetic Heat Conductivity in CaCu_2O_3 . *Phys. Rev. Lett.* *98*, 027201. 10.1103/PhysRevLett.98.027201.
21. Berggold, K., Lorenz, T., Baier, J., Kriener, M., Senff, D., Roth, H., Severing, A., Hartmann, H., and Freimuth, A. (2006). Magnetic heat transport in R_2CuO_4 ($\text{R} = \text{La}, \text{Pr}, \text{Nd}, \text{Sm}, \text{Eu}, \text{and Gd}$). *Phys. Rev. B.* *73*, 104430. 10.1103/PhysRevB.73.104430.
22. Hess, C., Baumann, C., Ammerahl, U., Büchner, B., Heidrich-Meisner, F., Brenig, W., and Revcolevschi, A. (2001). Magnon heat transport in $(\text{Sr}, \text{Ca}, \text{La})_{14}\text{Cu}_{24}\text{O}_{41}$. *Phys. Rev. B.* *64*, 184305. 10.1103/PhysRevB.64.184305.
23. Kawamata, T., Kaneko, N., Uesaka, M., Sato, M., and Koike, Y. (2010). Enhancement of thermal conductivity due to spinons in the one-dimensional spin system SrCuO_2 . *J. Phys. Conf. Ser.* *200*, 022023. 10.1088/1742-6596/200/2/022023
24. Hlubek, N., Zotos, X., Singh, S., Saint-Martin, R., Revcolevschi, A., Büchner, B., and Hess, C. (2012). Spinon heat transport and spin–phonon interaction in the spin-1/2 Heisenberg chain cuprates Sr_2CuO_3 and SrCuO_2 . *J. Stat. Mech.* *2012*, P03006. 10.1088/1742-5468/2012/03/P03006.
25. Sun, X. F., Takeya, J., Komiya, S., and Ando, Y. (2003). Thermal conductivity of lightly Sr- and Zn-doped La_2CuO_4 single crystals. *Phys. Rev. B. Condens Matter Mater Phys* *67*, 6. 10.1103/PhysRevB.67.104503.
26. Matsukawa, M., Mizukoshi, T., Noto, K., and Shiohara, Y. (1996). In-plane and out-of-plane thermal conductivity of a large single crystal of $\text{YBa}_2\text{Cu}_3\text{O}_{7-x}$. *Phys. Rev. B.* *53*, R6034–R6037. 10.1103/PhysRevB.53.R6034.
27. Morelli, D. T., Doll, G. L., Heremans, J., Peacor, S. D., Uher, C., Dresselhaus, M. S., Cassanho, A., Gabbe, D. R., and Jenssen, H. P. (1989) Thermal properties of single-crystal lanthanum cuprates at very low temperature. *Phys. Rev. B.* *39*, 804–807. 10.1016/0038-1098(91)90573-E.